https://doi.org/10.5194/amt-2022-321
Preprint. Discussion started: 14 February 2023

Atmospheric Measurement Techniques Discussions

Evaluation of the quality of a UAV-based eddy covariance system for measurements of wind and turbulent flux

Yibo Sun[1], Xinwen Lin[4], Bing Geng[5], Bo Liu[1,2,3], Shennan Ji[1,2,3]

[1]State Key Laboratory of Environmental Criteria and Risk Assessment, Chinese Research Academy of Environmental Sciences, Beijing 100012, China.
[2]Institute of Ecology, Chinese Research Academy of Environmental Sciences, Beijing 100012, China.
[3]State Environmental Protection Key Laboratory of Ecological Regional Processes and Functions Assessment, Beijing 100012, China.
[4]Collage of Geography and Environment Science, Zhejiang Normal University, Zhejiang 321004, China
[5]Beijing Academy of Social Sciences, 100101, Beijing, China.

Correspondence to: Yibo Sun (sunyb68@163.com)

Abstract. Instrumentation packages of eddy covariance (EC) have been developed for a small unmanned aerial vehicle (UAV) to measure the turbulent fluxes of latent heat (LE), sensible heat (H), and CO_2 (Fc) in the atmospheric boundary layer. This study evaluates the measurement performance of this UAV-based EC system. First, the precision (1σ) of the measurements was estimated at 0.04 m s^{-1} for wind velocity, 0.08 μmol m^{-2} s for Fc, 1.61 W m^{-2} for H, 0.15 W m^{-2} for LE, and 0.02 m s^{-1} for friction velocity (u*). Second, the effect of calibration parameter and aerodynamic characteristics of the UAV on the quality of the measured wind was examined by conducting a set of calibration flights. The results shown that the calibration improved the quality of measured wind field, and the influence of upwash and leverage effect can be ignored in the wind measurement. Third, data from the standard operational flights are used to assess the influence of resonance on the measurements and to test the sensitivity of the system by adding an error of ± 30 % to their calibrated value. Results shown that the effect of resonance mainly affect the measurement of CO_2 (~5 %). The pitch offset angle (ε_θ) significantly affected the measured vertical wind (~30 %) and H (~25 %). The heading offset angle (ε_ψ) only affected the horizontal wind (~15 %), and other calibration parameters had no significant effect on the measurements. The results lend confidence to use the UAV-based EC system, and suggest future directions for optimization and development of the next generation system.

1 Introduction

In environmental, hydrological and climate change sciences, the measurement of surface fluxes at the regional scale (kilometers level) has attracted great interest despite often being considered a gordian knot (Mayer et al., 2022; Chandra et al., 2022). Process-based or remote sensing (RS)-based models are often used to estimate surface fluxes of matter and energy at continental to global scales with typical spatial resolution from 1-10 km (Hu and Jia, 2015; Mohan et al., 2020; Liu et al., 1999). However, observational data, especially at similar scales, are often lacking, which presents a significant challenge for the validation and evaluation of the surface flux products from these models' estimates (Li et al., 2018; Li et al., 2017). On the

https://doi.org/10.5194/amt-2022-321
Preprint. Discussion started: 14 February 2023

ground, in past decades, extensive ground eddy-covariance (EC) flux sites with their networks and optical-microwave scintillometer (OMS) sites have been built to provide temporally continuous monitoring of surface fluxes at local (hundreds of meters around the measurement site of ground EC) and path (a distance of a few hundred meters to near 10 kilometers between transmitter and receiver terminal of OMS) scales (Yang et al., 2017; Liu et al., 2018; Zhang et al., 2021). Fluxes from ground measurements need to be scaled up to kilometers-scale to provide comparable spatial surface "relative-truth" flux data for the process- or RS-based models at larger spatial scales (Liu et al., 2016). However, the spatial density of these flux sites is still low compared to the complex variability of surface fluxes, which means that major scaling bias may exist in the upscaled flux data (Wang et al., 2016). Therefore, regional-scaled flux measurements are needed to be complement the ground- and models-based approaches (Vellinga et al., 2010).

The aircraft-based EC flux measurement method, which has been developed for turbulence measurements for more than 40 years (Lenschow et al., 1980; Desjardins et al., 1982), is considered as the optimum method to measure turbulent flux at regional scale (several hundred square kilometers), thus bridging the scale gap between ground and model-derived methods (Gioli et al., 2004; Garman et al., 2006). To date, several types of aircrafts, including manned or unmanned fixed-wing aircrafts, delta-wing aircrafts, and helicopters, have been used for measurements of turbulent flux by equipping them with the EC sensors to measure three-dimensional (3D) wind and gas concentrations at high frequency (Gioli et al., 2006; Metzger et al., 2012; Thomas et al., 2012; Bange and Roth, 1999). Among them, fixed-wing aircrafts and delta-wing aircrafts are better airborne platforms for EC measurements compared to helicopters due to their tightly coupled structure with the wind sensor and because their flow distortion around the fuselage can be more easily modeled (Prudden et al., 2018; Garman et al., 2008). A wide range of manned aircrafts has been developed to measure turbulent flux, including single-engine light aircrafts (e.g., Sky Arrow 650, Long-EC, WSMA) (Gioli et al., 2006; Crawford and Dobosy, 1992; Metzger et al., 2012), twin-engine aircrafts (e.g., Twin Otter, NASA CARAFE) (Desjardins et al., 2016; Wolfe et al., 2018) and larger quad-engine utility aircrafts (e.g., NOAA WP-3D) (Khelif et al., 1999). These airborne flux measurements, in combination with ground measurements, provide an excellent opportunity to produce regional-scaled, spatio-temporal surface flux datasets that can improve our understanding of the interactive processes between the land surface and the atmosphere in regional and global change (Chen et al., 1999; Liu et al., 1999; Prueger et al., 2005). However, manned aircrafts are expensive to operate and maintain. Aviation safety and operational regulations require that manned aircrafts must fly above a minimum altitude (400 m above the highest elevation within 25 km on each side of the center line of the air route) and must avoid hazardous conditions such as icing or severe turbulence (Elston et al., 2015). The flow distortion induced by the aircraft itself (from the wings, fuselage, and the propellers) complicates the wind vector measurement, which means that sophisticated correction procedures should be applied to compensate for the flow distortion effects (Elston et al., 2015; Williams and Marcotte, 2000; Drüe and Heinemann, 2013).

In recent years, interest in unmanned aerial vehicle (UAV) fixed-wing platforms for atmospheric studies has been fast growing, especially because of their lower construction, operation, and maintenance costs compared with manned platforms. High-performance fixed-wing UAVs offer a high payload capacity (5-10 kg) and similar endurance (2-3 h) and operating altitude (up to 3500 m above the sea level) to manned aircrafts, but with much less turbulence disturbance due to their small

https://doi.org/10.5194/amt-2022-321
Preprint. Discussion started: 14 February 2023

fuselage size (Reineman et al., 2013). More importantly, the advancements in small, fast, and powerful sensors and microprocessors make it possible to use of UAVs for comprehensive atmospheric measurements (Sun et al., 2021a). Several UAVs with different turbulence measurement objectives have been developed and deployed, ranging from small payload capacity (e.g., 140 g SUMO) to medium (e.g., 1.5 kg M^2AV, 1.0 kg MASC) and large (e.g., 6.8 kg Manta, 5.6 kg ScanEagle) (Reuder et al., 2016; Båserud et al., 2016; Van Den Kroonenberg et al., 2012; Reineman et al., 2013). A comprehensive overview of the use of these UAVs for turbulence sampling can be found in Elston et al. (2015) and Sun et al. (2021a). For turbulence measurements, the UAVs were equipped with a commercial or custom multi-hole (5- or 9-hole) probe paired with an integrated navigation system to obtain the wind vector. Small and medium UAVs typically could only measure fast 3D wind vector and air temperature fluctuations for measurements of momentum and sensible heat flux, whereas, large UAVs were equipped with more types (e.g., radiation, image, or gas concentration) and more accurate sensors for measurement of a larger range of meteorological properties including sensible and latent heat fluxes, radiation fluxes as well as surface properties (Reineman et al., 2013; Sun et al., 2021a). UAVs equipped with scientific instruments can be deployed in a variety of application environments and conditions. UAVs offer distinct advantages over manned aircraft in their ability to safely perform measurements and greatly reduce operational costs especially in low-altitude conditions (below 100 m above the ground level), which are optimal for measuring turbulent flux (Witte et al., 2017). Anderson and Gaston (2013) predict that UAVs will revolutionize the spatial data collection in ecology and meteorology.

The EC method is a well-developed technology for directly measuring vertical turbulent flux (flux of heat, matter and momentum) within the atmospheric boundary layers (ABL) (Peltola et al., 2021). It requires accurate time (for ground tower) or spatial (for mobile platform) series of both the transported scalar quantity and the transporting turbulent wind. Each should be measured at sufficient frequency to resolve the flux contribution from small eddies (Vellinga et al., 2013). The measurement of the geo-referenced 3D wind vector, which is the prerequisite for EC measurements, is challenging. Airborne measurement of geo-referenced 3D wind is the vector sum between the aircraft velocity relative to the earth (inertial velocity) and the velocity relative to the air (relative wind vector, or true airspeed). Therefore, accurate measurements of the relative wind as well as the motion and attitude of the platform are essential to accurately measure the geo-referenced wind vector and turbulent flux (Metzger et al., 2011). Garman et al. (2006) estimated the 1σ precision of the vertical wind measurements of a commercial 9-hole turbulence probe (known as "Best Air Turbulence Probe", often abbreviated as the "BAT Probe") to be 0.03 m s^{-1} by combining the precision of the BAT Probe and the integrated navigation device. The BAT Probe is widely used on manned fixed-wing aircrafts, such as Sky Arrow 650 ERA (Environmental research aircraft), Beechcraft Duchess, and Diamond DA42, for turbulent flux measurement (Gioli et al., 2006; Garman et al., 2008; Sayres et al., 2017). A light delta-wing EC flux measurement aircraft developed by Metzger et al. (2011) reported a 1σ precision of wind of 0.09 m s^{-1} for horizontal wind an 0.04 m s^{-1} for vertical wind. The 1σ precision of flux measurement was 0.003 m s^{-1} for friction velocity, 0.9 W m^{-2} for sensible heat flux, and 0.5 W m^{-2} for latent heat flux. The smallest resolvable magnitudes for the wind velocity and turbulent flux were estimated from these values by assuming a signal-to-noise ratio of 5:1 (Metzger et al., 2012). The EC flux measurement from a UAV platform can now be achieved with a similar reliability to a manned platform. The Manta and ScanEagle UAV-based

https://doi.org/10.5194/amt-2022-321
Preprint. Discussion started: 14 February 2023

EC measurements developed by Reineman et al. (2013) achieved precise wind measurements (0.05 m s^{-1} for horizontal and 0.02 m s^{-1} for vertical wind) using a custom nine-hole probe and a commercial high precision integrated navigation system (INS), at a lower price and lighter weight than the commercial BAT probe. However, the onboard instrument packages for Manta and ScanEagle UAV are independent of each other in their measurements of turbulent and radiation flux, and the CO_2 flux measurement is lacking.

Inspired by these studies, Sun et al. (2021a) used a high-performance fuel-powered vertical take-off and landing (VTOL), fixed-wing platform to integrate the scientific payloads for EC and radiation measurements to obtain a comprehensive measurement of turbulent and radiation flux using an UAV. This UAV-based EC system measured turbulent fluxes including sensible heat, latent heat, and CO_2, as well as radiation including net radiation and upward- and downward-looking photosynthetically active radiation (PAR). This system was successfully tested in the Inner Mongolia of China and applied to measure the regional sensible and latent heat fluxes in the Yancheng coastal wetland in Jiangsu, China (Sun et al., 2021a; 2021b). During these field studies, the UAV-based EC measurements achieved a near consistent observational result compared with ground EC measurements. However, some shortcomings in the developed UAV-based EC system were also identified. In particular, the noise effects from the engine and propeller were not fully isolated, resulting in high frequency noise in the measured scalars (air temperature, H_2O, and CO_2 concentration). This UAV-based EC system is being continuously improved (in Section 2.1) based on previous field measurements. However, there is no quantitative evaluation of the measurement capability of the wind field and turbulent flux or of the influence of the resonance from the UAV-based EC measurement system. Previous work using ground EC measurements as a benchmark to assess the measurement performance of the UAV-based EC has been disputed, due to difference in EC sensors, platforms, measurement height, and source areas (i.e., footprint), as well as the influence of surface heterogeneity, flux divergence, inversion layer and the stochastic nature of turbulence (Sun et al., 2021b; Wolfe et al., 2018; Hannun et al., 2020).

This study attempts to quantitatively evaluate the performance of a UAV-based EC system in the measurement of wind field and turbulent fluxes. First, the study investigates the 1σ measurement error of the geo-referenced wind vector and turbulent flux by propagating the error of each EC sensor along the data process procedure. Then, a set of calibration flights were conducted to assess how the calibration parameters and aerodynamic characteristics of the UAV affect the quality of the wind measurement. The effects of resonance noise on the measured scalar variance and the fluxes were also estimated by comparing the real (co)spectra curve with the theoretical reference curve from Massman and Clement (2005). Lastly, the sensitivity of the measured geo-referenced wind vector and turbulent flux to the calibration parameters (determined by the calibration flight) were assessed by adding an error of ±30 % to their optimum calibration values.

https://doi.org/10.5194/amt-2022-321
Preprint. Discussion started: 14 February 2023

Atmospheric Measurement Techniques Discussions

2 Materials and Methods

2.1 The UAV-based EC system

The UAV platform used for EC measurement is a high-performance, fuel-powered VTOL, fixed-wing UAV, which has minimal requirements for the takeoff location and offers a high payload capacity of up to 10 kg. The UAV has a wing-span of 3.7 m, a fuselage length of 2.85 m, and a maximum take-off weight of 60 kg. The UAV engine is mounted in a pusher configuration, allowing for the turbulence probe to be installed directly on the nose of the UAV, minimizing or eliminating airflow contamination due to upwash and sidewash generated by the wings (Crawford et al., 1996). Control of the UAV is totally autonomous, and the pilots have the option to enable manual and semi-manual control in emergency conditions. The UAV has a cruise flight speed of 28 to 31 m s^{-1} with an endurance of almost 3 h, and it has a flight ceiling of up to 3800 m above sea level. Detailed information on this UAV could be found in Sun et al. (2021a).

The flux payloads of the UAV-based EC system include a precision-engineered 5-hole pressure probe (5HP) for measurement of the true airspeed and the attack (α) and sideslip (β) angles of incoming flow relative to the UAV, a dual-antenna integrated navigation system (INS) for high accuracy measurement of ground speed and attitude, an open path infrared gas analyzer (IRGA) for recording the atmospheric densities of CO_2 and water vapor, a fast temperature sensor for measurement of the fast temperature fluctuations, and a slow-response temperature probe for providing a mean air temperature reference. The auxiliary payloads include a net radiometer and two photosynthetically active radiation (PAR) radiometers that look upward and downward. The sample rate of the flux payloads is 50 Hz except for the slow-response temperature probe (1 Hz), yielding a turbulence horizontal resolution of approximately 1.2 m at a cruising speed of 30 m s^{-1}. The system was improved according to deficiencies identified after several field measurements with the following adjustments: 1) a laser distance measurement unit was mounted for measuring the distance between the UAV and the ground level, 2) the platinum resistance thermometer was replaced by a thermocouple (Omega T-type COCO-003; $\emptyset 0.075$ mm) for improving the resistance of the high-frequency temperature measurements to vibration noise from the engine, 3) the vibration isolator structure of the IRGA was improved, and 4) the original datalogger (CR1000X, Campbell, USA) was replaced with a lighter one (CR6, Campbell, USA). All the digital and analog signals from the measurement sensors are stored and synchronized by the on-board datalogger, and the on-board scientific payloads are designed to be isolated from the electronic components of the UAV to ensure that any problems occurring would not jeopardize the safety of the UAV (Sun et al., 2021a).

In the present study, to estimate the 1σ precision for the measured geo-referenced wind and turbulent flux, the sensor modules and the 1σ precision of measurement variables related to EC measurement were used, as presented in Table 1. For the 5HP, the 1σ precision was acquired from the wind tunnel test after the wind tunnel calibration (Sun et al., 2021a).

Table 1: The sensor modules, measured variables, and their 1σ precision used to determine the geo-referenced wind velocity and turbulent flux.

Sensor (Module)	Variables	Precision ($\mathbf{1\sigma}$)

https://doi.org/10.5194/amt-2022-321
Preprint. Discussion started: 14 February 2023

Atmospheric Measurement Techniques Discussions

GNSS/INS (Trimble BD992-INS)	Roll, Pitch, Heading	0.1°
	Horizontal velocity	0.007 m s^{-1}
	Vertical velocity	0.02 m s^{-1}
5HP (Simtec AG ADP-55)	Attack angle	0.02°#
	Sideslip angle	0.04°#
	True airspeed	0.05 m s^{-1}#
	Static pressure	1.1 hPa
	Dynamic pressure	0.003 hPa
IRGA (Campbell EC150)	CO_2 density	0.2 mg m^{-3}
	H_2O density	0.004 g m^{-3}
Thermistor (BetaTherm 100K6A1IA)	Temperature (slow)	0.2 °C
Thermocouple (Omega T-type COCO-003)	Temperature (fast)	0.5 °C

Results from the wind tunnel test.

2.2 Field campaign

2.2.1 In-flight calibration campaign

An in-flight calibration campaign was carried out on 4 September 2022 at the Caofeidian Shoal Harbor (39°2′55″ N, 118°38′48″ E) in the Bohai Sea of northern China. The average water depth of this area is approximately 0-5 m, with a maximum water depth of 22 m. At low tide, a large area of the tidal flat is exposed; while at high tide, only the barrier islands are visible (Xu et al., 2021). The optimum atmospheric conditions for the in-flight calibration include 1) no large turbulent transport, 2) a constant mean horizontal wind, and 3) mean vertical wind near zero (Van Den Kroonenberg et al., 2008). These conditions are easier to meet over the sea surface than land, due to the uniform nature of the sea surface. Additionally, the sea-atmosphere interaction is relatively weaker than the land-atmosphere interaction (Mathez and Smerdon, 2018).

The in-flight calibration campaign included three flight maneuvers, including a 'box' maneuver, 'racetrack' maneuver, and 'acceleration-deceleration' maneuver. The trajectory of the calibration flight is shown in Figure 1, with different color corresponding to different flight maneuvers. The calibration flight was executed between 7:28-7:48 a.m. (CST) to coincide with the ebb tide stage. During this time, the average water depth was approximately 1.1 m, and the average flight altitude was 400 m ($\sigma = \pm 0.78$ m) above the sea level. Considering the conditions of the regional underlying surface and the stable atmospheric conditions in the early morning, we assume no disturbance from underlying surface was present during the calibration flight.

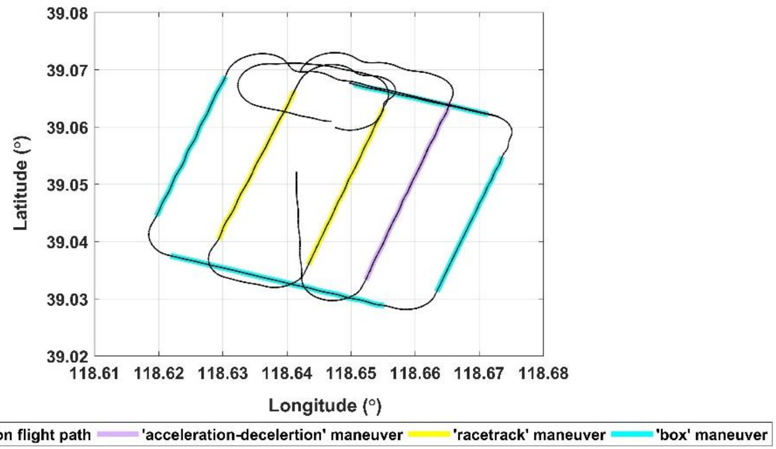

Figure 1. Flight trajectory of the calibration campaign on 4 September 2022 at the Caofeidian Shoal Harbor in the Bohai Sea of northern China.

In this study, the 'box' maneuver is used to determine the mounting misalignment angle in the heading (ϵ_ψ) and pitch (ϵ_θ) between the 5HP and the center of gravity (CG) of the UAV. The flight path is a box in which the four straight legs are flown at constant cruising speed, flight altitude, and heading for 2 minutes. The 'racetrack' maneuver is used to evaluate the quality of the calibration parameters acquired from the previous 'box' maneuver. The flight path consists of two parallel straight flight tracks connected by two 180^o turns. Each straight flight section lasts 2 minutes at constant speed and flight altitude. Lastly, the 'acceleration-deceleration' maneuver is used to check the influence of lift-induced upwash from the wing to the measured attack angle by the 5HP. During this maneuver, the aircraft is kept straight and level at constant pressure altitude. When beginning this maneuver, the aircraft accelerates to its maximum airspeed (35 m s^{-1}). Then, the airspeed reduces gradually to near its minimum airspeed (25 m s^{-1}) and back up to its maximum airspeed. The pressure-altitude of the aircraft is maintained throughout this maneuver, and the entire maneuver lasts one minute. This maneuver creates a series continuous changed pitch (θ) and attack (α) angle. A relationship between the measured incident flow attack angles (α) by the 5HP and the measured pitch angle by the INS of close to 1:1, indicates that the effect from the fuselage-induced flow distortion on the wind measurements is negligible (Garman et al., 2006).

2.2.2 Standard operation flight campaign

Previous studies have shown that the measured scalars were affected by the vibration noise from the engine and propeller of the UAV (2021b; Sun et al., 2021a). In order to evaluate the effects of resonance on the measured scalar and to investigate the sensitivity of the measured geo-referenced wind and turbulent flux to uncertainty in the calibration parameters, we used data from 7 flights in the Dagang district (38°54′27″ N, 117°48′16″ E) in Tianjin, China between 8 and 16 August 2022. This area is located on the west coast of the Bohai Sea and is a coastal alluvial plain with altitudes between 1-3 m (Chen et al., 2017). The flight path, shown in Figure 2, includes three parallel transect lines of approximately 4 km in length each and at 1-2 km intervals. All flights were performed in the same trajectory at low altitude about 90 m above sea level. The flight area covered three different underlying surfaces: land, coastal zone, and water surfaces.

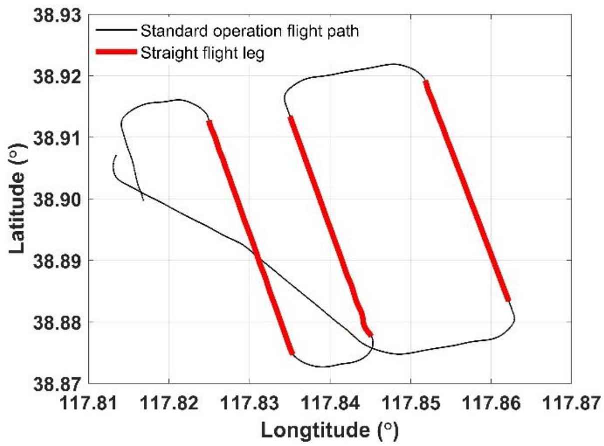

Figure 2. Flight trajectory of the standard operation flight campaign, 8-16 August 2022, at Dagang district, Tianjin, China.

During the operation flight campaign, the atmospheric stability conditions changed from stable (Monin-Obukhov stability parameter, $z/L = 1.93$) to very unstable ($z/L = -10.28$) as measured by the UAV. The average net radiation of each transect line changed from -40 W m^{-2} over the sea surface to 626 W m^{-2} over the land surface. These flight data provide various measurement conditions to evaluate the performance of the UAV-based EC system.

2.3 Data processing

The raw data collected with the on-board datalogger (CR6, Campbell, USA) is subsequently saved in Network Common Data Form (netCDF) format. It includes dynamic and static pressure, attack, and sideslip angle of incoming flow; slow (1 Hz) and fast (50 Hz) air temperature; mass concentration of H_2O and CO_2; as well as the full navigation data (including 3D location, ground speed, angular velocity, and attitude, etc.) of the UAV. Before processing the raw data into geo-referenced wind vector and turbulent flux, a moving average filter was used to detect outliers in each variable. Detected outliers were removed and replaced by values obtained by linear interpolation. Outliers tend to be rare. However, if outliers constitute more than 20 % of the data points, the corresponding flight data should be discarded. The cleaned raw data was then used to calculate the geo-referenced wind vector, (co)spectra, and turbulent fluxes.

2.3.1 Wind measurements

The full form of the equations of motion for calculating the geo-referenced wind vector by our UAV-based EC system is described in detail in Supplement. From the aircraft platform, turbulent wind is measured in two independent reference coordinate systems: the relative true airspeed ($\widehat{U}_a$) measurement in the aircraft coordinate system and the ground speed of the aircraft (U_p) in the geo-referenced coordinate system. The geo-referenced wind (U) is the vector sum of the relative true airspeed ($\widehat{U}_a$), the UAV's motion (U_p) and the tangential velocity due to the rotational motion of the aircraft ("lever arm" effect), which is described in Eq. (S2).

The relative wind vector ($\widehat{U}_a$) measured by the aircraft is susceptible to flow distortion because the airplane must distort the flow to generate lift and thrust, and the aircraft's propellers, fuselage, and wings are the main sources of flow distortion as flow barriers (Metzger et al., 2011). For fixed-wing aircrafts, the wind probe mounted on the nose of the UAV and extended as far forward of the fuselage as possible could avoid significant influence from flow distortion from the fuselage and propellers. Nevertheless, the wind measurement is still subject to lift induced upwash due to the wings distorting the flow to generate lift and thrust. The influence of upwash decreases with linear distance from the wing and appears as an additional vertical component of airflow ahead of the wind probe (Crawford et al., 1996; Garman et al., 2008). The magnitude of upwash influence generally increases with airplane size and airspeed, typically ranging from 0.5 to 2.5 m s^{-1} as reported by the manned fixed-wing aircraft (Garman et al., 2008). Therefore, for EC measurements by manned fixed-wing aircrafts, the upwash effects must be corrected for wind measurements (Garman et al., 2008; Kalogiros and Wang, 2002). However, wind measurements using a multi-hole probe on the UAV seldom need this correction due to the fuselage size and because the airspeed is very low compared to a manned aircraft. This is considered in the equations for relative wind calculation (in Supplement) used in this study as well. The 'acceleration-deceleration' flight maneuver (Section 2.2.1) was used to assess whether the lift-induced upwash could be safety ignored by the UAV-based EC system.

The lever arm effects due to the spatial separation between the tip of the wind probe and the CG of UAV can influence the wind measurements (Eqs. S15 to S17). Typically, the separation distance (L) is small, and the influence of the lever arm effects can be ignored when the L is less than about 10 m (Lenschow, 1986). In the current UAV-based EC system, the displacements of the 5HP tip with respect to the CG of the UAV along the three axes of UAB body coordinate are: $x^b = 1.459$ m, $y^b = 0$ m, and $x^b = 0.173$ m (in Supplement); thus, the influence of leverage effects in geo-referenced wind calculation was also ignored. This was confirmed by assessing the difference in the geo-referenced wind vectors with and without the correction term.

2.3.2 Spectra and turbulent flux calculation

Unlike traditional ground-based EC measurements, those recorded on aircraft platforms are subject to several simultaneous motions, including flow distortion around the fuselage and resonance from the rotation of the engine and propeller. Spectral analysis is an effective way to assess if and to what extent the UAV's motion influences the EC measurements. For this reason, the fast Fourier transform (FFT) method was used to calculate the spectra and co-spectra of the measured turbulent variables. Before calculating the turbulence (co)spectra, condition of the raw turbulence data was performed, including a linear detrend and tapering using the Hamming window to reduce the spectral leakage (sharp edge) according to Kaimal et al. (1989).

Based on EC technology and spatial averaging, the turbulent flux is calculated using covariances of vertical wind (w) with horizontal wind components (u, v) for vertical flux of momentum (τ), with virtual potential temperature (θ_v) for sensible heat flux (H), with water vapor density (q) for latent heat flux (LE), and with CO_2 density (c) for CO_2 flux (F_c). The time lag due

https://doi.org/10.5194/amt-2022-321
Preprint. Discussion started: 14 February 2023

to the separation between the 5HP tip, the adjacent temperature probe, and the open-path gas analysis did not need to be corrected because the time delay was less than 1 second at the cruise airspeed of 30 m s^{-1} and sensor separation less than 20 cm. Detailed information about the EC method and airborne EC calculation can be found in other studies (Aubinet et al., 2012; Vellinga et al., 2013; Gioli et al., 2006).

One important aspect of airborne EC measurement is the definition of a proper spatial averaging length to calculate turbulent flux (Sun et al., 2018). Such spatial averaging length depends on the flying altitude, surface characteristics, and atmospheric stability, and could be determined using Ogive analysis (Gioli et al., 2004; Kirby et al., 2008). In this study, the objective is not to quantify the actual flux exchange between the surface and the atmosphere, but rather to assess the sensitivity of the calculated turbulent flux to external parameters. Therefore, the entire measurement data of each straight and level flight leg (each with length about 4 km) from the standard operational flight campaign was used to calculate turbulent flux, regardless of the uncertainty of the flux results.

2.4 Evaluation strategy

2.4.1 Propagation of sensor errors

The EC technique relies upon the precise measurement of the geo-referenced wind vector and atmospheric scalars. Measured from an aircraft, determining the geo-referenced wind vector requires a sequence of thermodynamic and trigonometric equations, and the calculation of turbulent flux also needs a series of data operations and corrections to the turbulent variables (Metzger et al., 2012). The EC data processing procedure and these equations propagate various sources of error to the measured geo-referenced wind vector and turbulent flux. To estimate the errors in the geo-referenced wind vector and turbulent flux, we performed a Monte Carlo simulation of the data processing procedure.

The Monte Carlo simulation method consists of repeated calculation of the target quantity, each time varying the input data randomly within their stated limits of precision. The distribution of the calculated quantity then shows the effects of the imprecision of the input data (Anderson, 1976). In this study, all input variables (Table 1) used to calculate the geo-referenced wind vector and turbulent flux were randomly sampled from the Gaussian distributions with means corresponding to the constant altitude straight line flight and one standard deviation (1σ) widths given by individual component typical precision specifications from the manufacturer. Errors in the input variables are considered uncorrelated. The Monte Carlo process was repeated $N = 10^5$ times, and the measurement precision of the geo-referenced wind vector and turbulent flux was estimated as the standard deviation of the distribution of the simulated results.

The Monte Carlo error simulation gives the nominal precision of the geo-referenced wind and turbulent flux, but does not consider the influence of environmental changes. Following the methods of Lenschow and Sun (2007), we assess whether the accuracy of wind measurements from the UAV in satisfying the minimum signal level needed for resolving the mesoscale variations of the three wind components in the encountered atmospheric conditions. Firstly, the minimum required signal level for measurement of vertical air speed (ω) under the encountered atmospheric conditions could be estimated as (Lenschow and Sun, 2007):

$$\frac{\partial w}{\partial t} < 0.2\sqrt{2}\sigma_w 2\pi k v_{tas} \quad (1)$$

with the true airspeed (v_{tas}) set to mean cruise speed 30 m s^{-1}, the peak signal magnitude (σ_w) of the power spectra, and the corresponding wavenumber (k) (Thomas et al., 2012). The measurement error of the system in the vertical wind component can be calculated as (Lenschow and Sun, 2007):

$$\frac{\partial w}{\partial t} \cong \Theta \frac{\partial v_{tas}}{\partial t} + v_{tas}\frac{\partial \Theta}{\partial t} + \frac{\partial w_{UAV}}{\partial t} \quad (2)$$

with $\Theta = \alpha - \theta$, where α is the attack angle, θ is the pitch angle, w_{UAV} is the UAV's vertical velocity. According to Lenschow and Sun (2007), the signal level and mesoscale fluctuation of horizontal wind components (u and v) are considerably larger than that of vertical wind, so the accuracy criteria are not nearly as stringent. The measurement error of the horizontal wind component could be calculated as (Lenschow and Sun, 2007):

$$\frac{\partial u}{\partial t} \cong -\frac{\partial v_{tas}}{\partial t} + \frac{\partial u_{UAV}}{\partial t} \quad (3)$$

$$\frac{\partial v}{\partial t} \cong \Psi \frac{\partial v_{tas}}{\partial t} + v_{tas}\frac{\partial \Psi}{\partial t} + \frac{\partial v_{UAV}}{\partial t} \quad (4)$$

and,

$$\Psi \equiv \psi' + \beta \quad (5)$$

where u_{UAV}, v_{UAV} are the UAV's horizontal velocity measured from INS, ψ' is the departure of the measured true heading from the average true heading, and β is the sideslip angle of airflow. If the measurement error of the 3D wind vector from Eqs. (2) to (4) is smaller than the required minimum signal level of the vertical and horizontal wind components, it can be confirmed that the measurement accuracy of the geo-referenced 3D wind vector from UAV is sufficient to resolve the mesoscale variations of the three wind components in the encountered atmospheric conditions.

2.4.2 Wind measurement evaluation

The key to successful aircraft EC measurements lies in the translation of accurately measured, aircraft-orientated, wind vectors to geo-referenced orthogonal wind vectors (Thomas et al., 2012). Accurate measurements of geo-referenced wind vectors typically depend on the measurement precision of the sensors (i.e., 5HP and INS), the quality of the calibration parameters, as well as the geometry structure of the UAV-based EC system (i.e., flow distortion and leverage effect). For evaluation of the effect of the latter two aspects, a calibration flight campaign (Section 2.2.1) was performed to determine the calibration parameter (ϵ_ψ, ϵ_θ), check its quality, as well as to ascertain the effects of the lever arm and up-wash by the wings. The methods for acquiring the calibration parameter were given by Vellinga et al. (2013) and Sun et al. (2021a), and the results are reported in Supplement (Figs. S2 and S3). In the in-flight calibration campaign, a 'racetrack' maneuver was performed to check the quality of the calibration parameter determined from the 'box' flight maneuver. The initial ($\epsilon_\psi = 0°, \epsilon_\theta = 0°$) and calibrated ($\epsilon_\theta = -0.183°, \epsilon_\psi = 2°$, in Supplement) set of parameters were used to calculate the geo-referenced wind vector. By comparing the mean and standard deviation of the horizontal and vertical wind vector between the initial and calibrated set, the quality of the geo-referenced wind vector measurement in real environment conditions can be verified.

Effects from the flow distortion around the body of the aircraft, especially the induced upwash by the wings, can significantly influence the correspondence between measured and free-stream flow variables (Garman et al., 2008). The induced upwash by the wings modifies the local angle of attack, causing the measured attack angle (α) to be larger than the free-stream attack angle (α_∞). According to Crawford et al. (1996), the pitch angle (θ) by the INS instrument can be utilized as an estimate of the free-stream attack angle (α_∞) if the aircraft's vertical velocity is zero, since it is unaffected by lift-induced upwash and varies directly with α_∞ when the ambient vertical wind is zero. Under ideal conditions (zero aircraft vertical velocity and zero ambient vertical wind), the approximation relationship of $\theta \cong \alpha_\infty$ is valid when $\theta < 6°$ (Crawford et al., 1996; Vellinga et al., 2013). Departures from the 1:1 relationship can be caused by airflow distortion around the airplane behind the 5HP. The 'acceleration-deceleration' maneuver (Section 2.2.1) produced various pitch and attack angles measured under various airspeeds, which allowed a direct comparison between the pitch angle (θ) and the attack angle (α). If the slope between α and θ is close to unity, it indicates that the influence of lift-induced upwash can be ignored; otherwise, its influence should be corrected using upwash models (Garman et al., 2006). At last, the influence of leverage effects was evaluated based on the measurement data from the 'acceleration-deceleration' maneuver (Section 2.2.2) by considering or ignoring the leverage effect correction term in Eqs. S15 to S17.

2.4.3 Resonance effects

Previous work found that the measurement of the atmospheric scalars (e.g., air temperature, H_2O, and CO_2 concentration) is susceptible to resonance effects caused by the operation of the engine and propeller (Sun et al., 2021b). In order to further reduce the resonance effects, the vibration damping structure of the developed UAV-based EC system was further optimized. The reference (co)spectra curve of Massman and Clement (2005) was used to quantify the influence of the resonance effects remaining after vibration isolation optimization. Massman and Clement (2005) gave the generalization mathematical expression of the models of spectra and co-spectra:

$$Co(f) = A_0 \frac{1/f_x}{[1+m(f/f_x)^{2\mu}]^{\frac{1}{2\mu}\left(\frac{m+1}{m}\right)}} \tag{6}$$

where f is frequency (Hz), f_x is the frequency at which $fCo(f)$ reaches its maximum value, A_0 is a normalization parameter, m is the (inertial subrange) slope parameter, and μ is the broadness parameter. To describe co-spectra, m should be 3/4; to describe spectra, m should be 3/2. According to Massman and Clement (2005), $\mu = 7/6$ under stable atmospheric condition and $\mu = 1/2$ under unstable atmospheric condition.

According to Sun et al. (2021b), the noise influence from resonance mainly appears in the high frequency domain, the frequency range of the noise region was artificially designated to $f > 8$ Hz for air temperature, $f = 1 \sim 5$ Hz for water vapor, and $f = 1 \sim 8$ Hz for CO_2. The normalized spectra and co-spectra curve were adopted and the area difference of the designated frequency range beneath the (co)spectra curve between the measured and reference (co)spectra curve was calculated to quantify the influence of resonance noise in the variance and flux of the measurement atmosphere scalars. An example is shown in Figure 3, and also shown is the reference (co)spectra curve of Massman and Clement (2005), with the (co)spectral maximum at $f_x = 0.1$. The red region in Fig. 3 represents the impact extent of the resonance noise in the variance (Figs. 3a to 3c) and fluxes (Figs. 3d to 3f) of the measured scalars. The systematic noise deviation in the fluxes of sensible, latent heat and CO_2 could be derived relative to the entire frequency range.

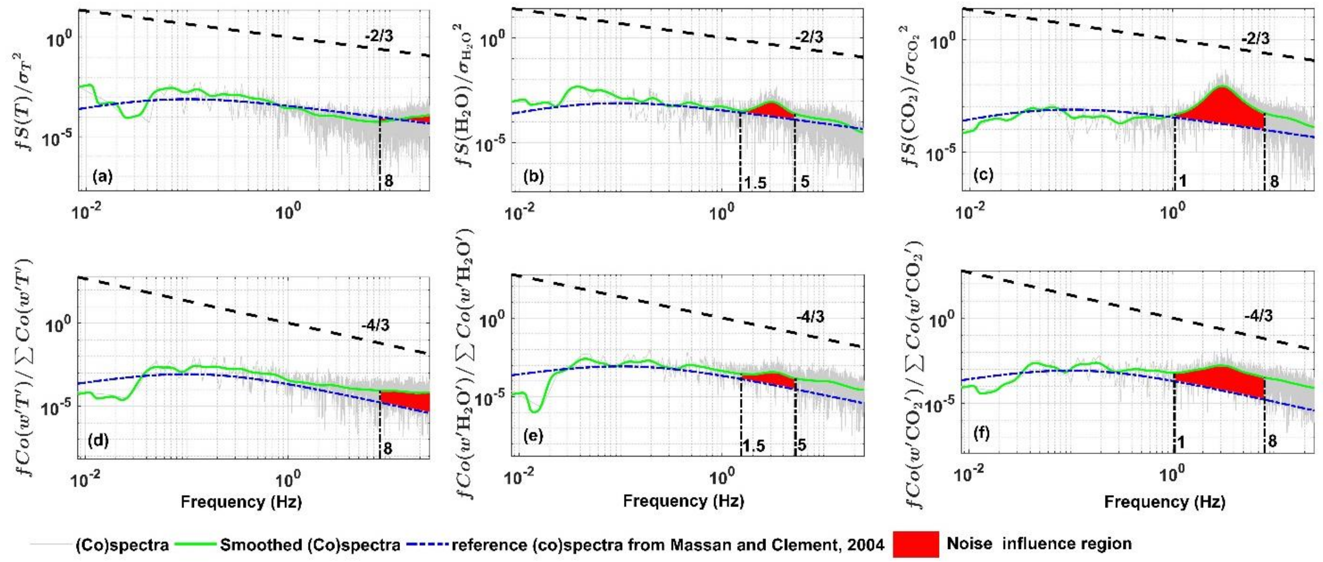

Figure 3. The influence of resonance noise on the spectra (top row) and co-spectra (bottom row) curve of the measured scalars based on the measurement from the standard operation flight campaign on 8 August 2022 at Dagang district, Tianjin, China. The red region is the area difference of the designated frequency range (vertical black dashed-dotted line) beneath the (co)spectral curve between the measured and reference (co)spectral curve.

2.4.4 Sensitivity analysis

To understand the relative influence of external calibration parameters on the measurements of geo-referenced wind vector and turbulent flux, a sensitivity analysis was conducted. The magnitude of the change in the wind vector and turbulent flux was investigated as a function of the uncertainties of four parameters: three mounting misalignment angles ($\epsilon_\psi, \epsilon_\theta, \epsilon_\phi$) between the 5HP and the CG of the UAV and one temperature recover factor ($\epsilon_r = 0.82$) used to calculate the ambient temperature (Eq. 3 in Sun et al. 2021a).

First, the sensitivity of the geo-referenced 3D wind vector and turbulent flux to the uncertainties of the individual parameter was investigated. The geo-referenced 3D wind vector and turbulent flux was calculated based on the straight leg (about 4 km) of the standard operational flight with an added error of ± 30 % to the calibrated value of each calibration parameter alternately except for ϵ_ϕ, for which the typical range of $\pm 0.9°$ was taken for sensitivity analysis (Vellinga et al., 2013).

Then, to test the overall interactions between the parameters, a second sensitivity test was run to calculate the geo-referenced 3D wind vector and turbulent flux using an error of ± 30 % added to all the calibration parameters simultaneously. Lastly, the relative errors of the calibrated set and the added error set of geo-referenced 3D wind vector and turbulent flux values was calculated to evaluate the perturbation of the wind vector and turbulent flux under the variation of each calibration parameter as well as under simultaneous variation of all calibration parameters. During the sensitivity analysis, the calculated geo-referenced wind and turbulent flux results whose absolute value was less than their least resolvable magnitude (in Table 2) were filtered out to avoiding the error contained in the measurement itself from impacting results.

2.4.5 Relative error

In this study, relative error (*RE*) was used to evaluate the influence of different factors on the measurements of geo-referenced wind vector and turbulent flux by the UAV-based EC system. It is defined as:

$$RE = \frac{|x_0|-|x|}{|x|} \times 100\ \% \tag{7}$$

where '| |' means the absolute value, x is the 'true' value, x_0 is the influence value. *RE* > 0 means the exerted influence will cause the measurement value to be larger than 'true' value and vice versa.

3 Results

3.1 Error analysis

After running $N = 10^5$ samples through the data processing procedure, the results of Monte Carlo error simulation for geo-referenced wind vector and turbulent flux are summarized in Table 2. The least resolvable magnitude of the measurements of wind and turbulent flux was calculated by assuming the minimum required signal-to-noise ratio of 5:1 (Metzger et al., 2012). The 1σ precision of the geo-referenced wind vector measurement was ± 0.04 m s^{-1} for the horizontal and vertical wind components, and the magnitude of the wind velocity greater than 0.2 m s^{-1} could be reliably measured. The calculated measurement 1σ precision of the geo-referenced vertical wind component agreed well with the 1σ uncertainty in the vertical wind measurement (0.057 m s^{-1}) calculated by propagating instrument errors through linear combination, as described by Sun et al. (2021a).

Table 2: Results of the simulated measurement precision (1σ) of the geo-referenced wind vector and turbulent flux from the Monte Carlo error simulation with N=10^5 runs and the least resolvable magnitude assuming the minimum required signal-to-noise ratio of 5:1.

https://doi.org/10.5194/amt-2022-321
Preprint. Discussion started: 14 February 2023

Atmospheric Measurement Techniques Discussions

Measurements	Measurement precision (1σ)	Least resolvable magnitude
u-windspeed (m s^{-1})	0.04	0.2
v-windspeed (m s^{-1})	0.03	0.15
w-windspeed (m s^{-1})	0.04	0.2
CO_2 flux (μmol m^{-2} s)	0.08	0.4
Sensible heat flux (W m^{-2})	1.61	8.05
Latent heat flux (W m^{-2})	0.15	0.75
Friction velocity (m s^{-1})	0.02	0.1

The simulated 1σ measurement precision of the turbulent flux was 0.08 μmol m^{-2} s for the CO_2 flux, 1.61 W m^{-2} for the sensible heat flux, 0.15 W m^{-2} for the latent heat flux, and 0.02 m s^{-1} for the friction velocity, respectively. Using a signal-to-noise ratio of 5:1, the minimum magnitudes for reliably resolving the CO_2 flux, friction velocity, sensible and latent heat fluxes were 0.4 μmol m^{-2} s, 0.1 m s^{-1}, 8.05 W m^{-2}, and 0.75 W m^{-2}, respectively.

The Monte Carlo error simulation gave the nominal precision that does not consider the influence of environmental conditions. Changes in the environment will lead to sensor drift, increasingly deteriorating the measurement with flight duration (Metzger et al., 2012; Lenschow and Sun, 2007). Following the methods of Lenschow and Sun (2007), the ability of the limitations of the accuracy of wind field measurements from UAV to resolve the mesoscale variations of the 3D wind components in the encountered atmospheric conditions was assessed. For the vertical wind, the mesoscale variability was defined as the peak signal magnitude of the power spectra curve. The corresponding average wavenumber was determined as 0.09 m^{-1} based on the straight flight leg (about 4 km, lasting about 120 s) of the standard operational flight. Then, the minimum required signal level for the vertical wind measurement was estimated as $\partial w/\partial t \simeq 0.14\ \mathrm{m\ s^{-2}}$. The accuracy of the vertical wind measurement using Eq. (2) is estimated as follows. The first term on the right-hand side of Eq. (2) is dominated by the drift in the differential pressure transducer, the value of $\partial v_{tas} = 0.05\ \mathrm{m\ s^{-1}}$ acquired from the wind tunnel test was applied (Table 1). The histogram of Θ derived from the standard operational flights is shown in Figure 4. The 99 % confidence interval indicates that the value of Θ seldom exceeds $\pm 3°$, i.e., ± 0.053 radians. Thus, the value of the first term was estimated as $2.2 \times 10^{-5}\ \mathrm{m\ s^{-2}}$.

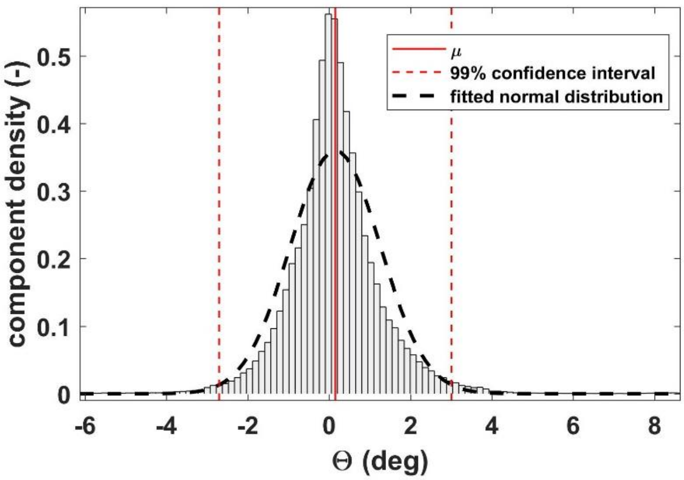

Figure 4. Histogram of Θ derived from the standard operational flight. Component density is scaled so that the histogram has a total area of one. Red vertical lines indicate distribution average (solid) and 99% confidence interval (dashed). The black dashed bell curve displays a reference fitted normal distribution.

The second term in Eq. (2) is a combination of INS pitch accuracy and drift in the measured attack angles. The combined accuracies of these two sensors were applied to derive $\partial\Theta = 0.0024$ radians. Thus, the second term in Eq. (2) was estimated as 6×10^{-4} m s^{-2}. Finally, the third term in Eq. (2) was estimated as 1.7×10^{-4} m s^{-2}, according to the stated accuracy of the vertical velocity from the INS. The overall performance of the vertical wind measurement (7.9×10^{-4} m s^{-2}) was accurate enough to resolve the mesoscale variations in vertical air velocity.

The required accuracy of horizontal wind for mesoscale measurement was estimated as 10 times larger than that of vertical wind, i.e., $\partial u/\partial t \simeq \partial v/\partial t \simeq 1.4$ m s^{-2}. The measurement accuracy of the horizontal wind component u was estimated as 4.8×10^{-4} m s^{-2} according to Eq. (3). Like the first term in Eq. (2), with the value of Ψ rarely exceeding ± 0.18 radians, the measurement accuracy of the horizontal wind component v was estimated as 2.7×10^{-2} m s^{-2}according to Eq. (4). Thus, the measurement accuracy of the horizontal wind components was accurate enough to resolve the mesoscale variations in the horizontal air velocity as well.

3.2 Wind measurement

The calibration results of the offset in pitch (ϵ_θ) and heading (ϵ_ψ) angles based on the 'box' maneuver are provided in Supplement (Figs. S2 and S3). The final calibration values are $\epsilon_\theta = -0.183°$ and $\epsilon_\psi = 2°$. In order to verify the quality of these calibration parameters, a 'racetrack' maneuver was performed. Figure 5 shows the verification results by plotting wind vectors and calculating summary statistics for the 'racetrack' maneuver (including turns), using the initial ($\epsilon_\theta = \epsilon_\psi = 0°$, Fig. 5a) and calibrated (Fig. 5b) set of parameters. The introduction of the calibration parameter effectively improved the quality of geo-referenced wind vector measurement. The standard deviation for wind direction, $\sigma_{U_{dir}}$, is 4.9° for the calibrated set compared to 8.7° for the initial set, and the standard deviation of wind speed, σ_U, is 0.52 m s^{-1} for the calibrated set compared to 1.12 m s^{-1} for the initial set. The average vertical wind speed is much closer to zero ($\overline{w} = -0.006$ m s^{-1}) for the calibrated set than for the initial set ($\overline{w} = 0.1$ m s^{-1}). For the horizontal wind, it is evident from Fig. 5 that the wind direction and velocity are little affected by sharp turns. On the contrary, the measurement of the vertical wind component is obviously affected by turns in flight, as shown by the large ripple in the vertical wind speed around the scan value of 150 (Fig. 5). It should be noted that the influence of upwash flow and the leverage effect are not considered in the calculated of geo-referenced wind vector.

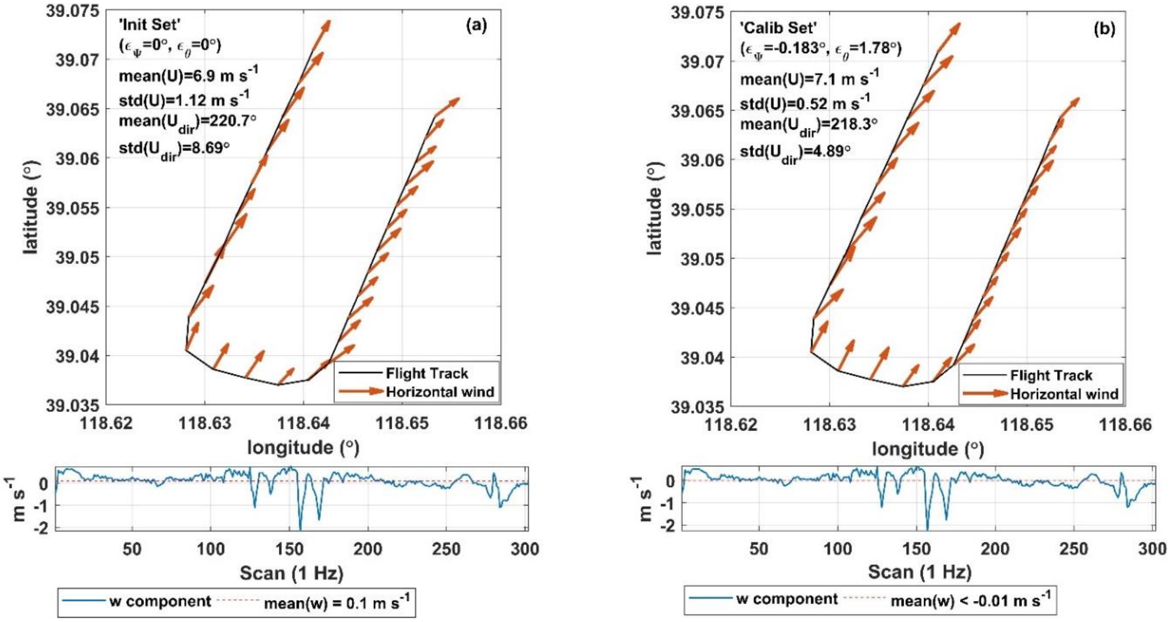

Figure 5. Quality check of the calibration parameter by plotting wind vectors and calculating summary statistics for the 'racetrack' maneuver, using the initial (a) and calibrated (b) set of parameters. The calibration flight was carried out on 4 September 2022 at the Caofeidian Shoal Harbor.

In order to check the influence of the lift-induced upwash on the attack angle measurement from the 5HP, an 'acceleration-deceleration' flight maneuver was performed. During the 'acceleration-deceleration' maneuver, INS data shown a vertical velocity of the UAV at 0.05±0.2 m s^{-1}, the altitude of UAV at 392±0.6 m, the heading of UAV at 199±2.4°. The flight conditions met the requirements of the 'acceleration-deceleration' maneuver (Vellinga et al., 2013). The relationship between the pitch angle (θ) measured by INS and the attack angle (α) measured by 5HP is plotted in Figure 6, where the attack angle was not corrected for lift-induced upwash. The slope (0.94) between θ and α is close to its theoretical value of 1, and the intercept (0.16) is close to zero. This result indicates that the lift-induced upwash has only a very small effect on the attack angle, and the influence of upwash could be ignored.

https://doi.org/10.5194/amt-2022-321
Preprint. Discussion started: 14 February 2023

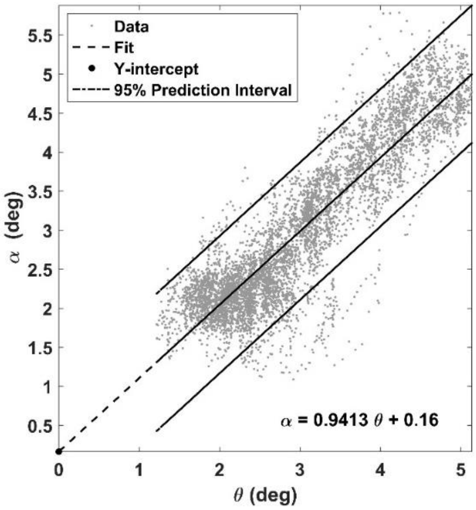

Figure 6. Relationship between the pitch angle (θ) measured by INS and the attack angle (α) measured by 5HP. The fitted linear equation is also shown.

Finally, the geo-referenced wind vector was calculated with and without the correction for the leverage effect based on the measurement data from the 'acceleration-deceleration' flight maneuver. The average relative differences between the corrected and uncorrected horizontal and vertical wind speeds are 0.1 % and 0.2 %, respectively. The standard deviation for horizontal wind speed is 0.307 m s^{-1} without the level arm term compared to 0.306 m s^{-1} when the level arm term is introduced. The standard deviation of vertical wind speed is 0.254 m s^{-1} without the level arm term compared to 0.253 m s^{-1} with the level arm term. The correction of leverage effect had minimal effect on improving the geo-referenced wind vector measurement; therefore, this correction term can be ignored.

3.3 Resonance noise

The resonance noise from the engine and propeller can lead to systematic overestimation of the variance and covariance of the observed atmospheric scalars. Since the noise mainly appears in the high frequency domain of the (co)spectra, the reference (co)spectral curve of Massman and Clement (2005) was used to quantify the systematically bias caused by the resonance noise.

All spectra curves of the variance of measured scalars (including air temperature, H_2O, and CO_2 concentration) approximately followed the reference spectra curve and the reference -2/3 slope in the inertial subrange (Figs. 3a to 3c). The largest scatter occurred in the spectra of CO_2 (Fig. 3c). When comparing the spectra curve with the reference spectra, the resonance noise led to a systematic deviation in the variance of air temperature, H_2O, and CO_2 concentration of 0.1±0.1 %, 1.0±0.79 %, and 4.4±0.66 %, respectively, relative to the entire frequency range. For the fluxes of sensible, latent heat and CO_2, all the co-spectra curves approximately follow the reference co-spectra curve and the reference -4/3 slope in the inertial subrange (Figs. 3d to 3f). Compared with the reference co-spectra, the resonance noise led to a systematic deviation in the flux of sensible, latent heat, and CO_2 of 0.07±0.004 %,0.3±0.25 %, and 2.9±1.62 %, respectively, relative to the entire frequency range.

The results show that resonance noise has a very little impact on the measured variance and fluxes. Among them, the measurements of CO_2 concentration and flux are most susceptible to the resonance noise, but the impact of this noise is limited to around 5 % of the observed value.

3.4 Sensitivity analysis

In this study, in order to investigate the sensitivity of the geo-referenced wind vector and turbulent flux measurements to the uncertainties of the external calibration parameter, a sensitivity test was conducted by adding an error of ± 30 % to the calibrated value of each calibration parameter. It is assumed that the maximum uncertainties contained in the calibration parameter is not more than 30 % of its own value.

First, the sensitivity of the geo-referenced 3D wind and turbulent flux to the uncertainties of the individual parameters was tested. The *RE* was used to quantify the sensitivity. Tables 3 and 4 show the *RE* results. For the measurement of the geo-referenced wind vector, Table 3 shows that the uncertainty in the temperature recovery factor (ε_r) and 5HP mounting misalignment error in the roll (ϵ_ϕ) angle do not contribute significantly to errors in the wind measurements, which were typically smaller than 4% of the observed value. The parameter ε_θ had the largest effect on the vertical wind component (up to 30 %), whereas ε_ψ had the largest effect on the horizontal wind component. For the measurement of turbulent flux, Table 4 shows that the errors in ε_r and ϵ_ϕ does not influence significantly the flux measurements (typically small than 5%). Calibration parameters ε_θ and ε_ψ had significant effects on the measurement of turbulent flux. Adding an error of ± 30 % to the calibration parameter ε_θ may result in significant uncertainty in the measured turbulent flux (large *RE* variance). Similarly, adding an error of ± 30 % to the calibration parameter ε_ψ resulted in the largest effect on latent heat fluxes (*RE* may up to 15 %).

Table 3: *RE* of the sensitivity test for the geo-referenced 3D wind vector (u, v, w). An error factor of ± 30 % was added to each calibrated parameter. The geo-referenced 3D wind vector was calculated based on the straight leg of the standard operational flight.

Parameter	Error (%)	*RE* of geo-referenced 3D wind vector mean ± std		
		u (%)	v (%)	w (%)
$\boldsymbol{\varepsilon_r}$	-30	0.04±0.41	-0.004±2	0±0
	30	0.06±0.43	0.27±1.1	-0.07±0.23
$\boldsymbol{\varepsilon_\varphi}$*	-30	0.41±2.51	-0.09±2.05	1.15±2.43
	30	-0.43±2.61	0.09±1.79	-1.1±2.66
$\boldsymbol{\varepsilon_\theta}$	-30	0.03±0.41	-0.35±2.54	-30.51±6.42
	30	0.05±0.45	0.42±1.82	30.37±6.61
$\boldsymbol{\varepsilon_\psi}$	-30	2.98±25.06	-2.04±16.3	0±0
	30	-2.97±24.96	2.42±16.63	0±0

* The optimum calibration value is set to 0, ε_φ was varied over $\pm 0.9°$, which is 30 % of its typical range.

https://doi.org/10.5194/amt-2022-321
Preprint. Discussion started: 14 February 2023

Atmospheric Measurement Techniques
Discussions

Table 4: *RE* of the sensitivity test for the turbulent fluxes. An error factor of ±30 % was added to each calibrated parameter. The turbulent fluxes were calculated based on the straight leg of the standard operational flight.

Parameter	Error (%)	*RE* of turbulent flux mean ± std			
		fCO2 (%)	H (%)	LE (%)	u* (%)
ε_r	-30	1.04±3.04	-0.76±4.82	0.1±0.29	0±0
	30	-1.0±3.3	0.74±4.8	-0.1±0.29	0.2±1.07
ε_φ*	-30	0.07±1.2	0.03±0.7	0.15±1.51	0.54±1.71
	30	-0.14±0.89	-0.06±0.7	-0.16±1.46	0.12±1.61
ε_θ	-30	-3.27±11.18	-0.8±9.48	0.19±11.91	-4.08±5.61
	30	2.34±10.52	-0.44±8.24	-1.27±9.92	3.73±4.53
ε_ψ	-30	1.78±5.18	-0.73±4.87	1.89±13.42	0.63±5.75
	30	-0.99±3.96	-0.57±3.26	2.66±11.76	-0.59±4.42

* See Table 3.

The overall sensitivity of the geo-referenced 3D wind vector and turbulent flux to the external calibration parameters was tested by adding an error of ±30 % to all the calibration members simultaneously. Tables 5 and 6 provided a summary of the *RE* results. For the measurement of geo-referenced wind vector (Table 5), adding an error of ±30 % to the calibration set at the same time resulted in a high *RE* (near 30 %) for vertical wind and a low *RE* (about 4%) for horizontal wind, which also had high *RE* variance (up to 28 %). For the measurement of turbulent fluxes, the measurement of the latent heat flux (mean *RE* > 6 %) is more sensitivity to the errors in the calibration parameter than other measurements (mean *RE* < 3 %) and had a larger *RE* variance (>10 %). In general, CO_2 and sensible heat fluxes as well as friction velocity are not sensitive to errors in the external calibration parameters, but there were also some exceptions where the response to errors was large (e.g., the *RE* variance of CO_2 flux up to 10 %).

Table 5: *RE* of the sensitivity test for the geo-referenced 3D wind vector (u, v, w) calculated by adding an error of ±30 % to all the calibrated parameter simultaneously. The geo-referenced 3D wind vector was calculated based on the straight leg of the standard operational flight.

Parameter	Error (%)	*RE* of geo-referenced 3D wind vector mean ± std		
		u (%)	v (%)	w (%)
All	-30	4.24±27.89	-3.2±21.1	-29.35±4.63
	30	-4.15±27.46	3.55±21.91	29.16±4.86

Table 6: *RE* of the sensitivity test for the turbulent flux calculated by adding an error of ±30 % to all the calibrated parameter simultaneously. The turbulent flux was calculated based on the straight flight leg of the standard operational flight.

Parameter	Error (%)	*RE* of turbulent flux mean ± std			
		fCO2 (%)	H (%)	LE (%)	u* (%)
All	-30	-1.19±10.51	-0.9±8.06	2.71±13.91	-2.92±8.19
	30	-0.49±10.01	-1.66±5.4	-6.07±13.24	1.74±6.55

https://doi.org/10.5194/amt-2022-321
Preprint. Discussion started: 14 February 2023

4 Discussions

As one in a new generation of airborne flux measurement platforms, the UAV-based EC system can significantly reduce the cost of implementing airborne flux measurement campaigns and greatly promote their wide application at regional scales. The trend of sensor miniaturization further promotes the rapid development of technology in this field. Sun et al. (2021a) developed an UAV-based EC system for measuring the turbulent flux of sensible heat, latent heat, CO_2, as well as radiation fluxes of net radiation and photosynthetically active radiation (PAR). This study aimed to quantitatively evaluate the performance of this system in the measurement of wind vector and turbulent flux.

First, the measurement precision (nominal precision) of the UAV-based EC system was evaluated by propagating the sensor errors to the geo-referenced wind vector and turbulent flux using Monte Carlo error simulation. The 1σ precision for geo-referenced wind measurement was estimated to be $\pm$0.04 m s^{-1}, and the 1σ precision for turbulent flux was 0.08 μmol m^{-2} s for the CO_2 flux, 1.61 W m^{-2} for the sensible heat flux, 0.15 W m^{-2} for the latent heat flux, and 0.02 m s^{-1} for the friction velocity. As proposed by Lenschow and Sun (2007), a minimum signal-to-noise ratio of 5:1 was assumed to be required to measure the wind field and turbulent flux. Using that ration, the least resolvable magnitude for wind and turbulent flux measurement was estimated at 0.2 m s^{-1} for wind velocity, 0.4 μmol m^{-2} s for the CO_2 flux, 8.05 W m^{-2} for the sensible heat flux, 0.75 W m^{-2} for the latent heat flux, and 0.1 m s^{-1} for the friction velocity. These derived minimum resolvable magnitudes for measurements of wind vector and turbulent flux can be used as a basic reference for the measurement capability of the UAV-based EC system, and the measured values of wind vector and scalar fluxes smaller than the minimum resolvable values should be considered unreliable. The accuracy of the sensors was also assessed by examining the collected data (Lenschow and Sun, 2007; Thomas et al., 2012). The overall performance of geo-referenced wind measurement is sufficient accuracy for resolving the mesoscale variations of the 3D wind components under the encountered atmospheric conditions. Therefore, it is possible to capture the mesoscale variability of the atmospheric boundary layer (ABL) over a wide range of spatial scales by performing longer flight paths.

Second, based on the measurement data from the in-flight calibration campaign, several key factors affecting the accuracy of geo-referenced wind measurement were analysed. First, the UAV-based EC system was calibrated (in Supplement) using data from the 'box' flight maneuver to correct the mounting misalignment between the 5HP and the CG of the UAV in the heading ($\epsilon_\theta = -0.183°$) and pitch ($\epsilon_\psi = 2°$) angles. The quality of the acquired calibration parameter was verified using the 'racetrack' flight maneuver, and the acquired calibration value effectively improved the observed wind field with smaller variance compared with the wind calculated using their initial value. The measured geo-referenced 3D wind vector was consistent with the assumptions made about the atmospheric condition for calibration campaign (constant horizontal wind and near zero mean vertical wind) especially in the standard operation flight. The measurement of the vertical wind component was significantly affected by the in-flight turn (maintaining about 20° roll). Therefore, it is necessary to avoid using the data from the turn section for turbulent flux calculation. Compared to the other studies (Vellinga et al., 2013; Reineman et al., 2013), the relatively large variance in the calibrated horizontal wind and wind direction may be caused by the nonstationary condition

https://doi.org/10.5194/amt-2022-321
Preprint. Discussion started: 14 February 2023

of the turbulence. This was caused by the reason that the flight altitude of 400 m was not high enough to avoid interaction from the underlying surface.

The current calibration procedure did not include methods to determine the offset angle in roll (ε_{φ}) and the temperature recovery factor (ε_r) because of the small vertical separation (27.3 cm) between the 5HP and the roll axis of the UAV and the small Mach number (<0.1) during operational flight. The default ($\varepsilon_{\varphi} = 0°$) and empirical ($\varepsilon_r = 0.82$) value were adopted for these calibration parameters. The sensitivity analysis shown these two parameters have no large effect on the wind vector and turbulent flux.

Wind measurements from the airborne platform may be susceptible to flow distortion and rigid-body rotation (leverage effects). However, the influence of these two aspects were ignored when calculating the geo-referenced wind vector. To confirm that these effects could be ignored, data from 'acceleration-deceleration' flight maneuver was used to analyse the effects of lift-induced upwash and the leverage effect on the wind measurements. The results demonstrate that the upwash has almost no effect on the wind measurement, which was indicated by the near 1:1 relationship (0.94) between the measured attack angles and pitch angle. The slight departures from the ideal 1:1 relationship may have been caused by the nonstationary condition during the flight. Differences were very minor between the 3D wind vector corrected and uncorrected for the leverage effect. Thus, ignoring the influence of the leverage effect has almost no effect on the measurement of wind. Therefore, the geo-referenced 3D wind vector can be measured reliably by the current UAV-based EC system without considering the possible disturbance from the lift-induced upwash and leverage effect as indicated by the results.

Third, because the UAV-based EC system has not completely insulated the noise from the operation of the engine and propeller and its effect on the measured scalars, the reference (co)spectra of Massman and Clement (2005) was used to quantify the effect of the resonance noise on the variance and flux of the measured scalars. Previous studies found that the influence of resonance noise mainly appears in the high frequency domain of the power spectra of the measured atmospheric scalars (e.g., air temperature, H_2O, and CO_2 concentration). The frequency range of the noise region was artificially designated for air temperature, water vapor and CO_2. By calculating the area difference of the designated frequency range beneath the (co)spectral curve between the measured and reference (co)spectral curves, the resonance effect could be quantified. The results shown that, overall, resonance noise has little impact on the variance and fluxes of the measured scalars. The measurements of CO_2 concentration and flux were the most susceptible to resonance noise, but the maximum effect was less than 5 %. It should be noted that this method may overestimate the deviation caused by resonance noise as indicated by the reference (co)spectra curve and the measured (co)spectra not fully overlapping in the inertial subrange (shown in Fig. 3).

Gas detection based on optical absorption methods can achieve fast and high precision gas concentration measurements, but they are extremely sensitive to vibration noise. However, due to the limited space inside the UAV, it is difficult to install all the hardware needed for a complex vibration isolation structure to effectively isolate the impact of vibration on the gas analyser. The weight and the aerodynamic shape of the UAV also present challenges. In the future, a new UAV-based EC system based on a pure electric UAV could be developed. The electro-powered UAV has similar performance to the current fuel-powered UAV but can minimize the impact of vibration noise from the engine and propeller rotation, which makes it possible to completely isolate the resonance effect using a simple vibration isolation structure. Electro-powered UAVs also have other advantages including larger wingspan (lower cruising speed), a constant CG position, and lower operational complexity compared to the current system.

Forth, a sensitivity test was conducted to assess the perturbation of the geo-referenced wind vector and turbulent flux under variation of each calibrated parameter around its calibrated value as well as under simultaneous variation of all calibrated parameters. The sensitivity analysis was carried out based on the straight flight leg (about 4 km) by adding an error of ± 30 % to the calibrated parameter value and then calculating the *RE* of the geo-referenced wind vector and turbulent flux between the calibrated and added error sets of results. Values less than the least resolvable magnitude were removed from the dataset. The results revealed that uncertainties in the temperature recovery factor (ε_r) and mounting offset in roll angle (ε_φ) do not significantly contribute to an error in the measurement of wind vector and fluxes. The typical *RE* for the geo-referenced wind measurements is less than 1.2 % with variance less than 3 %, and the typical *RE* for turbulent flux is less than 1.1 % with variance less than 5 %. The sign of the added errors of ε_φ and ε_r also has no significant effect on the sign of the *RE*. Calibration parameters that had the largest effect on the measurement of geo-referenced wind vector and turbulent flux are the mounting offset angle in pitch (ε_θ) and heading (ε_ψ). Uncertainties in ε_θ had a direct effect on the vertical wind component, and these then propagate to the measured fluxes, resulting in a large fluctuation in the *RE* (~12 %). A negative error of the ε_θ resulted in smaller vertical wind and vice versa. Uncertainties in ε_ψ directly affect the measurement of the horizontal wind, and to some extent, the measurement of turbulent flux. The most obvious phenomenon is that the added error in ε_ψ lead to a great variability (up to 25 %) in the *RE* of horizontal wind. By checking the relationship between the magnitude of the horizontal wind (u, v) and *RE*, a near exponential relationships was seen. As shown in Figure 7, the influence of the error in the ε_ψ decreased significantly with the increase in horizontal wind velocity. Additionally, the measurement of latent heat flux may be greatly affected by the error in ε_ψ, which is reflected by the relatively large deviancy (~14 %) of the *RE*.

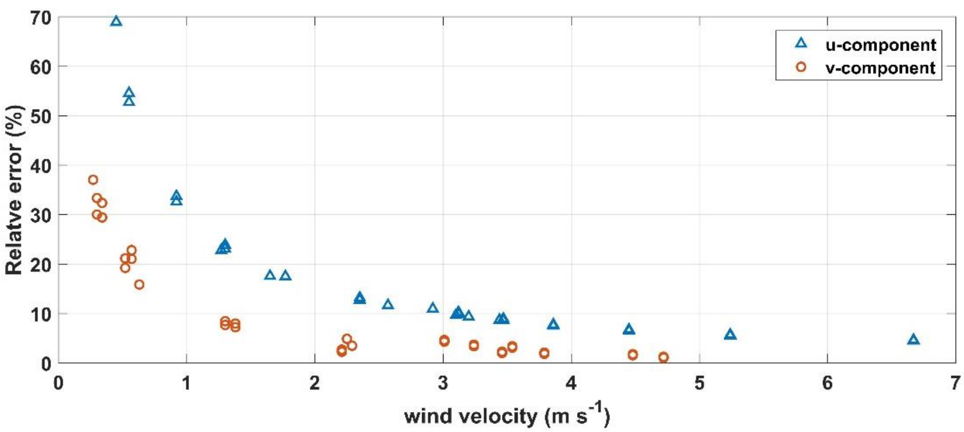

Figure 7. Relationship between the horizontal wind velocity (u, v) and *RE*. Wind velocity of less than 0.2 m s^{-1} was excluded.

https://doi.org/10.5194/amt-2022-321
Preprint. Discussion started: 14 February 2023

The second sensitivity test varied all the external calibration parameters simultaneously, which resulted in a slightly larger but similarly varied REs compared with the first test. The results confirm that the quality of calibration parameter ε_θ and ε_ψ had the largest effect on the reliability of measurement for geo-referenced wind vector and turbulent flux. The parameter ε_θ directly affected the measurement of vertical wind and propagated its errors to the measured turbulent flux. The parameter ε_ψ significantly affected the measurement of horizontal wind, and in the measurement of turbulent flux, its effect on latent heat flux was somewhat more pronounced than for other fluxes. Therefore, these two parameters need to be carefully calibrated.

Lastly, it should be noted that this study could not evaluate the accuracy of the measured geo-referenced wind vector and turbulent flux by the UAV-based EC system compared to their actual true value. An effective way to evaluate the measurement accuracy of this new technique is by comparing measured values with those from the traditionally recognized measurement. However, the direct comparison of flux measurements between aircraft and traditional ground tower is still challenging due to the difference in the measurement height, mechanism (time series for ground EC and space series for aircraft), and instruments (e.g., wind sensor). Previous studies have extensively compared the measurement of fluxes and wind vector between airborne and ground-based EC methods and found consistent results (Gioli et al., 2004; Metzger et al., 2012; Sun et al., 2021b). At the same time, substantial and consistent over- or underestimation of the measured wind and fluxes by UAV compared to ground measurements were observed and reported. These differences may be due to several factors such as vertical flux divergence (the measurement height of UAV is higher than ground-tower), surface heterogeneity (induced by the larger footprint region of the UAV compared to the ground tower), measurement errors (e.g., window length, resonance noise, etc.) as well as their difference in platform and sensors. Therefore, it is necessary to conduct a comparison test on the same platform and under the same environment to exclude the influence of these factors. Inspired by Reineman et al. (2013), future work can include developing a ground-vehicle-based UAV flux validation platform. This platform could carry both the UAV-based and traditional ground EC system to assess the measurement accuracy of the UAV-based EC system with the measurement of ground EC as the benchmark in a flight-like scenario.

5 Conclusions and further works

The main objective of this study was to quantitatively evaluate the performance of the developed UAV-based EC system in the measurement of geo-referenced wind vector and turbulent flux. In terms of measuring precision, turbulence measurements from the UAV-based EC system were achieved with sufficient precision to enable reliable measurement of geo-referenced wind and EC flux. Magnitudes larger than 0.2 m s^{-1} for wind velocity, 0.4 μmol m^{-2} s for CO_2 flux, 8.05 W m^{-2} for sensible and latent heat flux, and 0.1 m s^{-1} for friction velocity could be reliably measured by the UAV-based EC system by assuming the minimum required signal-to-noise ratio of 5:1 for EC application. Based on the data from the calibration flight, the carefully calibrated offset angle in pitch (ϵ_θ) and heading (ϵ_ψ) were shown to effectively improve the quality of wind field measurements, and the influences of flow distortion and the leverage effect on the wind measurement were minimal and could be ignored.

Atmospheric Measurement Techniques
Open Access
EGU
Discussions

The influence of resonance noise was small on the measurement of air temperature and water vapor (typically < 1 % for their variance and flux), but relatively large on the measurement of CO_2 (around 5 % for variance and flux).

The relevance of the uncertainties in the external calibration parameters ($\varepsilon_r, \epsilon_\phi, \varepsilon_\psi, \varepsilon_\theta$) to the computation of geo-referenced wind vector and turbulent flux was also assessed based on a sensitivity test. The measurements of the geo-referenced wind vector and turbulent flux were insensitive to the errors in the ε_r and ϵ_ϕ. The uncertainties in calibration parameter ε_θ and ε_ψ had the strongest effects. Because ε_θ directly effects vertical wind, its error will create inaccuracies in vertical wind measurement and then propagate the errors to the measurement of turbulent flux. The uncertainties in ε_ψ have a direct effect on the measurement of horizontal wind, and to some extent, the measurement of turbulent flux. Therefore, these two calibration parameters need to be carefully calibrated. Conducting the UAV-based EC measurement when wind velocity is larger than 1 m s^{-1} can led to more stable and reliable results of the wind speed measurement compared to a relatively windless environmental (< 1 m s^{-1}).

The developed UAV-based EC system measured the geo-referenced wind vector and turbulent flux with sufficient precision. The lift-induced upwash and leverage effect had almost no effect on the measurement of geo-referenced wind vector. The resonance effect caused by the operation of engine and propeller mainly affected the measurement of CO_2, and its effect on variance and flux was around 5 %. The quality of calibration parameters ε_ψ and ε_θ has a significant effect on the measurement of the geo-referenced wind vector and turbulent flux, underscoring the importance of careful calibration. Future research may include the development of a new generation UAV-based EC system with the following improvements: 1) a new electro-powered UAV platform with the advantages of being quieter (low noise), having a low cruising speed, and being easy to operate; 2) a ground-vehicle-based validation platform to enable direct comparative evaluation of the UAV-based EC system with traditional ground EC methods under near-identical environmental conditions; 3) a graphics based real-time monitoring system to make it possible to change the flight pattern according to real-time data. Ultimately, the versatility of the UAV-based EC system as a low cost and widely applicable environmental research aircraft facilitates further improving our understanding of the energy and matter cycling processes at regional scales.

Author contributions. SY, GB and LX planned the field campaign; SY, LB and JS carried out the field measurements. SY analysed the data and wrote the manuscript draft. GB and LX reviewed and edited the manuscript.

Competing interests. The authors declare that they have no conflict of interest.

Acknowledgments. This work was supported by the National Natural Science Foundation of China (Grant No. 42101477). We would like to thank F-EYE UAV Technology Co. Ltd. for building, maintaining, and operating the UAV in this study.

Data availability. Data for this research are not publicly available due to its proprietary nature currently. The UAV calibration flight data and the standard operation flight data in this study are available upon request to the corresponding author.

https://doi.org/10.5194/amt-2022-321
Preprint. Discussion started: 14 February 2023

Atmospheric Measurement Techniques
Discussions

References

Anderson, G. M.: Error propagation by the Monte Carlo method in geochemical calculations, Geochimica et Cosmochimica Acta, 40, 1533-1538, https://doi.org/10.1016/0016-7037(76)90092-2, 1976.

Anderson, K. and Gaston, K. J.: Lightweight unmanned aerial vehicles will revolutionize spatial ecology, Frontiers in Ecology and the Environment, 11, 138-146, https://doi.org/10.1890/120150, 2013.

Aubinet, M., Vesala, T., and Papale, D.: Eddy Covariance: A Practical Guide to Measurement and Data Analysis, Springer Atmospheric Sciences, Springer Netherlands, XXII, 438 pp., 10.1007/978-94-007-2351-1, 2012.

Bange, J. and Roth, R.: Helicopter-Borne Flux Measurements in the Nocturnal Boundary Layer Over Land – a Case Study, Boundary-Layer Meteorology, 92, 295-325, 10.1023/A:1002078712313, 1999.

Båserud, L., Reuder, J., Jonassen, M. O., Kral, S. T., Paskyabi, M. B., and Lothon, M.: Proof of concept for turbulence measurements with the RPAS SUMO during the BLLAST campaign, Atmos. Meas. Tech., 9, 4901-4913, 10.5194/amt-9-4901-2016, 2016.

Chandra, N., Patra, P. K., Niwa, Y., Ito, A., Iida, Y., Goto, D., Morimoto, S., Kondo, M., Takigawa, M., Hajima, T., and Watanabe, M.: Estimated regional CO2 flux and uncertainty based on an ensemble of atmospheric CO2 inversions, Atmos. Chem. Phys., 22, 9215-9243, 10.5194/acp-22-9215-2022, 2022.

Chen, J. M., Leblanc, S. G., Cihlar, J., Desjardins, R. L., and MacPherson, J. I.: Extending aircraft- and tower-based CO2 flux measurements to a boreal region using a Landsat thematic mapper land cover map, Journal of Geophysical Research: Atmospheres, 104, 16859-16877, https://doi.org/10.1029/1999JD900129, 1999.

Chen, W., Wang, D., Huang, Y., Chen, L., Zhang, L., Wei, X., Sang, M., Wang, F., Liu, J., and Hu, B.: Monitoring and analysis of coastal reclamation from 1995–2015 in Tianjin Binhai New Area, China, Scientific Reports, 7, 3850, 10.1038/s41598-017-04155-0, 2017.

Crawford, T. L. and Dobosy, R. J.: A sensitive fast-response probe to measure turbulence and heat flux from any airplane, Boundary-Layer Meteorology, 59, 257-278, 10.1007/BF00119816, 1992.

Crawford, T. L., Dobosy, R. J., and Dumas, E. J.: Aircraft wind measurement considering lift-induced upwash, Boundary-Layer Meteorology, 80, 79-94, 10.1007/BF00119012, 1996.

Desjardins, R. L., Brach, E. J., Alvo, P., and Schuepp, P. H.: Aircraft Monitoring of Surface Carbon Dioxide Exchange, Science, 216, 733-735, 10.1126/science.216.4547.733, 1982.

Desjardins, R. L., Worth, D. E., MacPherson, J. I., Bastian, M., and Srinivasan, R.: Flux measurements by the NRC Twin Otter atmospheric research aircraft: 1987–2011, Adv. Sci. Res., 13, 43-49, 10.5194/asr-13-43-2016, 2016.

Drüe, C. and Heinemann, G.: A Review and Practical Guide to In-Flight Calibration for Aircraft Turbulence Sensors, Journal of Atmospheric and Oceanic Technology, 30, 2820-2837, 10.1175/JTECH-D-12-00103.1, 2013.

https://doi.org/10.5194/amt-2022-321
Preprint. Discussion started: 14 February 2023

Atmospheric Measurement Techniques Discussions

Elston, J., Argrow, B., Stachura, M., Weibel, D., Lawrence, D., and Pope, D.: Overview of Small Fixed-Wing Unmanned Aircraft for Meteorological Sampling, Journal of Atmospheric and Oceanic Technology, 32, 97-115, 10.1175/JTECH-D-13-00236.1, 2015.

Garman, K. E., Wyss, P., Carlsen, M., Zimmerman, J. R., Stirm, B. H., Carney, T. Q., Santini, R., and Shepson, P. B.: The Contribution of Variability of Lift-induced Upwash to the Uncertainty in Vertical Winds Determined from an Aircraft Platform, Boundary-Layer Meteorology, 126, 461-476, 10.1007/s10546-007-9237-y, 2008.

Garman, K. E., Hill, K. A., Wyss, P., Carlsen, M., Zimmerman, J. R., Stirm, B. H., Carney, T. Q., Santini, R., and Shepson, P. B.: An Airborne and Wind Tunnel Evaluation of a Wind Turbulence Measurement System for Aircraft-Based Flux Measurements, Journal of Atmospheric and Oceanic Technology, 23, 1696-1708, 10.1175/JTECH1940.1, 2006.

Gioli, B., Miglietta, F., Vaccari, F. P., and Zaldei, A.: The Sky Arrow ERA, an innovative airborne platform to monitor mass, momentum and energy exchange of ecosystems, Annals of Geophysics, 49, 109-116, 10.4401/ag-3159, 2006.

Gioli, B., Miglietta, F., De Martino, B., Hutjes, R. W. A., Dolman, H. A. J., Lindroth, A., Schumacher, M., Sanz, M. J., Manca, G., Peressotti, A., and Dumas, E. J.: Comparison between tower and aircraft-based eddy covariance fluxes in five European regions, Agricultural and Forest Meteorology, 127, 1-16, https://doi.org/10.1016/j.agrformet.2004.08.004, 2004.

Hannun, R. A., Wolfe, G. M., Kawa, S. R., Hanisco, T. F., Newman, P. A., Alfieri, J. G., Barrick, J., Clark, K. L., DiGangi, J. P., Diskin, G. S., King, J., Kustas, W. P., Mitra, B., Noormets, A., Nowak, J. B., Thornhill, K. L., and Vargas, R.: Spatial heterogeneity in CO2, CH4, and energy fluxes: insights from airborne eddy covariance measurements over the Mid-Atlantic region, Environmental Research Letters, 15, 035008, 10.1088/1748-9326/ab7391, 2020.

Hu, G. and Jia, L.: Monitoring of Evapotranspiration in a Semi-Arid Inland River Basin by Combining Microwave and Optical Remote Sensing Observations, Remote Sensing, 7, 10.3390/rs70303056, 2015.

Kaimal, J. C., Clifford, S. F., and Lataitis, R. J.: Effect of finite sampling on atmospheric spectra, Boundary-Layer Meteorology, 47, 337-347, 10.1007/BF00122338, 1989.

Kalogiros, J. A. and Wang, Q.: Aerodynamic Effects on Wind Turbulence Measurements with Research Aircraft, Journal of Atmospheric and Oceanic Technology, 19, 1567-1576, 10.1175/1520-0426(2002)019<1567:AEOWTM>2.0.CO;2, 2002.

Khelif, D., Burns, S. P., and Friehe, C. A.: Improved Wind Measurements on Research Aircraft, Journal of Atmospheric and Oceanic Technology, 16, 860-875, 10.1175/1520-0426(1999)016<0860:IWMORA>2.0.CO;2, 1999.

Kirby, S., Dobosy, R., Williamson, D., and Dumas, E.: An aircraft-based data analysis method for discerning individual fluxes in a heterogeneous agricultural landscape, Agricultural and Forest Meteorology, 148, 481-489, https://doi.org/10.1016/j.agrformet.2007.10.011, 2008.

Lenschow, D. H.: Aircraft Measurements in the Boundary Layer, in: Probing the Atmospheric Boundary Layer, edited by: Lenschow, D. H., American Meteorological Society, Boston, MA, Boston, https://doi.org/10.1007/978-1-944970-14-7_5, 1986.

Lenschow, D. H. and Sun, J.: The spectral composition of fluxes and variances over land and sea out to the mesoscale, Boundary-Layer Meteorology, 125, 63-84, 10.1007/s10546-007-9191-8, 2007.

https://doi.org/10.5194/amt-2022-321
Preprint. Discussion started: 14 February 2023

Atmospheric Measurement Techniques Discussions

Lenschow, D. H., Delany, A. C., Stankov, B. B., and Stedman, D. H.: Airborne measurements of the vertical flux of ozone in the boundary layer, Boundary-Layer Meteorology, 19, 249-265, 10.1007/BF00117223, 1980.

Li, X., Liu, S., Xiao, Q., Ma, M., Jin, R., Che, T., Wang, W., Hu, X., Xu, Z., Wen, J., and Wang, L.: A multiscale dataset for understanding complex eco-hydrological processes in a heterogeneous oasis system, Scientific Data, 4, 170083, 10.1038/sdata.2017.83, 2017.

Li, X., Liu, S., Li, H., Ma, Y., Wang, J., Zhang, Y., Xu, Z., Xu, T., Song, L., Yang, X., Lu, Z., Wang, Z., and Guo, Z.: Intercomparison of Six Upscaling Evapotranspiration Methods: From Site to the Satellite Pixel, Journal of Geophysical Research: Atmospheres, 123, 6777-6803, https://doi.org/10.1029/2018JD028422, 2018.

Liu, J., Chen, J. M., Cihlar, J., and Chen, W.: Net primary productivity distribution in the BOREAS region from a process model using satellite and surface data, Journal of Geophysical Research: Atmospheres, 104, 27735-27754, https://doi.org/10.1029/1999JD900768, 1999.

Liu, S., Xu, Z., Song, L., Zhao, Q., Ge, Y., Xu, T., Ma, Y., Zhu, Z., Jia, Z., and Zhang, F.: Upscaling evapotranspiration measurements from multi-site to the satellite pixel scale over heterogeneous land surfaces, Agricultural and Forest Meteorology, 230-231, 97-113, https://doi.org/10.1016/j.agrformet.2016.04.008, 2016.

Liu, S., Li, X., Xu, Z., Che, T., Xiao, Q., Ma, M., Liu, Q., Jin, R., Guo, J., Wang, L., Wang, W., Qi, Y., Li, H., Xu, T., Ran, Y., Hu, X., Shi, S., Zhu, Z., Tan, J., Zhang, Y., and Ren, Z.: The Heihe Integrated Observatory Network: A Basin-Scale Land Surface Processes Observatory in China, Vadose Zone Journal, 17, 180072, https://doi.org/10.2136/vzj2018.04.0072, 2018.

Massman, W. and Clement, R.: Uncertainty in Eddy Covariance Flux Estimates Resulting from Spectral Attenuation, in: Handbook of Micrometeorology: A Guide for Surface Flux Measurement and Analysis, edited by: Lee, X., Massman, W., and Law, B., Springer Netherlands, Dordrecht, 67-99, 10.1007/1-4020-2265-4_4, 2005.

Mathez, E. and Smerdon, J.: Climate Change3. Ocean– Atmosphere Interactions, in: The Science of Global Warming and Our Energy Future, Columbia University Press, 69-100, doi:10.7312/math17282-005, 2018.

Mayer, J., Mayer, M., Haimberger, L., and Liu, C.: Comparison of Surface Energy Fluxes from Global to Local Scale, Journal of Climate, 35, 4551-4569, 10.1175/JCLI-D-21-0598.1, 2022.

Metzger, S., Junkermann, W., Butterbach-Bahl, K., Schmid, H. P., and Foken, T.: Measuring the 3-D wind vector with a weight-shift microlight aircraft, Atmos. Meas. Tech., 4, 1421-1444, 10.5194/amt-4-1421-2011, 2011.

Metzger, S., Junkermann, W., Mauder, M., Beyrich, F., Butterbach-Bahl, K., Schmid, H. P., and Foken, T.: Eddy-covariance flux measurements with a weight-shift microlight aircraft, Atmos. Meas. Tech., 5, 1699-1717, 10.5194/amt-5-1699-2012, 2012.

Mohan, M. M. P., Rajitha, K., and Murari, R. R. V.: Review of approaches for the estimation of sensible heat flux in remote sensing-based evapotranspiration models, Journal of Applied Remote Sensing, 14, 1-31, 10.1117/1.JRS.14.041501, 2020.

Peltola, O., Aslan, T., Ibrom, A., Nemitz, E., Rannik, Ü., and Mammarella, I.: The high-frequency response correction of eddy covariance fluxes – Part 1: An experimental approach and its interdependence with the time-lag estimation, Atmos. Meas. Tech., 14, 5071-5088, 10.5194/amt-14-5071-2021, 2021.

Prudden, S., Fisher, A., Marino, M., Mohamed, A., Watkins, S., and Wild, G.: Measuring wind with Small Unmanned Aircraft Systems, Journal of Wind Engineering and Industrial Aerodynamics, 176, 197-210, https://doi.org/10.1016/j.jweia.2018.03.029, 2018.

Prueger, J. H., Hatfield, J. L., Parkin, T. B., Kustas, W. P., Hipps, L. E., Neale, C. M. U., MacPherson, J. I., Eichinger, W. E., and Cooper, D. I.: Tower and Aircraft Eddy Covariance Measurements of Water Vapor, Energy, and Carbon Dioxide Fluxes during SMACEX, Journal of Hydrometeorology, 6, 954-960, 10.1175/JHM457.1, 2005.

Reineman, B. D., Lenain, L., Statom, N. M., and Melville, W. K.: Development and Testing of Instrumentation for UAV-Based Flux Measurements within Terrestrial and Marine Atmospheric Boundary Layers, Journal of Atmospheric and Oceanic Technology, 30, 1295-1319, 10.1175/JTECH-D-12-00176.1, 2013.

Reuder, J., Båserud, L., Jonassen, M. O., Kral, S. T., and Müller, M.: Exploring the potential of the RPA system SUMO for multipurpose boundary-layer missions during the BLLAST campaign, Atmos. Meas. Tech., 9, 2675-2688, 10.5194/amt-9-2675-2016, 2016.

Sayres, D. S., Dobosy, R., Healy, C., Dumas, E., Kochendorfer, J., Munster, J., Wilkerson, J., Baker, B., and Anderson, J. G.: Arctic regional methane fluxes by ecotope as derived using eddy covariance from a low-flying aircraft, Atmos. Chem. Phys., 17, 8619-8633, 10.5194/acp-17-8619-2017, 2017.

Sun, Y., Jia, L., Chen, Q., and Zheng, C.: Optimizing Window Length for Turbulent Heat Flux Calculations from Airborne Eddy Covariance Measurements under Near Neutral to Unstable Atmospheric Stability Conditions, Remote Sensing, 10, 10.3390/rs10050670, 2018.

Sun, Y., Ma, J., Sude, B., Lin, X., Shang, H., Geng, B., Diao, Z., Du, J., and Quan, Z.: A UAV-Based Eddy Covariance System for Measurement of Mass and Energy Exchange of the Ecosystem: Preliminary Results, Sensors, 21, 10.3390/s21020403, 2021a.

Sun, Y., Sude, B., Geng, B., Ma, J., Lin, X., Hao, Z., Jing, W., Chen, Q., and Quan, Z.: Observation of the winter regional evaporative fraction using a UAV-based eddy covariance system over wetland area, Agricultural and Forest Meteorology, 310, 108619, https://doi.org/10.1016/j.agrformet.2021.108619, 2021b.

Thomas, R. M., Lehmann, K., Nguyen, H., Jackson, D. L., Wolfe, D., and Ramanathan, V.: Measurement of turbulent water vapor fluxes using a lightweight unmanned aerial vehicle system, Atmos. Meas. Tech., 5, 243-257, 10.5194/amt-5-243-2012, 2012.

van den Kroonenberg, A., Martin, T., Buschmann, M., Bange, J., and Vörsmann, P.: Measuring the Wind Vector Using the Autonomous Mini Aerial Vehicle M2AV, Journal of Atmospheric and Oceanic Technology, 25, 1969-1982, 10.1175/2008JTECHA1114.1, 2008.

van den Kroonenberg, A. C., Martin, S., Beyrich, F., and Bange, J.: Spatially-Averaged Temperature Structure Parameter Over a Heterogeneous Surface Measured by an Unmanned Aerial Vehicle, Boundary-Layer Meteorology, 142, 55-77, 10.1007/s10546-011-9662-9, 2012.

https://doi.org/10.5194/amt-2022-321
Preprint. Discussion started: 14 February 2023

Vellinga, O. S., Dobosy, R. J., Dumas, E. J., Gioli, B., Elbers, J. A., and Hutjes, R. W. A.: Calibration and Quality Assurance of Flux Observations from a Small Research Aircraft*, Journal of Atmospheric and Oceanic Technology, 30, 161-181, 10.1175/JTECH-D-11-00138.1, 2013.

Vellinga, O. S., Gioli, B., Elbers, J. A., Holtslag, A. A. M., Kabat, P., and Hutjes, R. W. A.: Regional carbon dioxide and energy fluxes from airborne observations using flight-path segmentation based on landscape characteristics, Biogeosciences, 7, 1307-1321, 10.5194/bg-7-1307-2010, 2010.

Wang, H., Jia, G., Zhang, A., and Miao, C.: Assessment of Spatial Representativeness of Eddy Covariance Flux Data from Flux Tower to Regional Grid, Remote Sensing, 8, 742, 2016.

Williams, A. and Marcotte, D.: Wind Measurements on a Maneuvering Twin-Engine Turboprop Aircraft Accounting for Flow Distortion, Journal of Atmospheric and Oceanic Technology, 17, 795-810, 10.1175/1520-0426(2000)017<0795:WMOAMT>2.0.CO;2, 2000.

Witte, B. M., Singler, R. F., and Bailey, S. C. C.: Development of an Unmanned Aerial Vehicle for the Measurement of Turbulence in the Atmospheric Boundary Layer, Atmosphere, 8, 10.3390/atmos8100195, 2017.

Wolfe, G. M., Kawa, S. R., Hanisco, T. F., Hannun, R. A., Newman, P. A., Swanson, A., Bailey, S., Barrick, J., Thornhill, K. L., Diskin, G., DiGangi, J., Nowak, J. B., Sorenson, C., Bland, G., Yungel, J. K., and Swenson, C. A.: The NASA Carbon Airborne Flux Experiment (CARAFE): instrumentation and methodology, Atmos. Meas. Tech., 11, 1757-1776, 10.5194/amt-11-1757-2018, 2018.

Xu, S., Xu, S., Zhou, Y., Yue, S., Zhang, X., Gu, R., Zhang, Y., Qiao, Y., and Liu, M.: Long-Term Changes in the Unique and Largest Seagrass Meadows in the Bohai Sea (China) Using Satellite (1974–2019) and Sonar Data: Implication for Conservation and Restoration, 10.3390/rs13050856, 2021.

Yang, X., Yong, B., Ren, L., Zhang, Y., and Long, D.: Multi-scale validation of GLEAM evapotranspiration products over China via ChinaFLUX ET measurements, International Journal of Remote Sensing, 38, 5688-5709, 10.1080/01431161.2017.1346400, 2017.

Zhang, G., Zhang, J., and Meng, P.: Estimation of kilometer-scale heat fluxes over a hilly area in Northern China using an optical-microwave scintillometer, Agricultural Water Management, 244, 106582, https://doi.org/10.1016/j.agwat.2020.106582, 2021.